nature communications



Article

https://doi.org/10.1038/s41467-025-61000-z

Marine phytoplankton and sea-ice initiated convection drive spatiotemporal differences in Arctic summertime mercury rebound

Received: 19 December 2024

Fange Yue ¹□, Hélène Angot ², Hongwei Liu & Zhouging Xie ¹□

Accepted: 10 June 2025

Published online: 02 July 2025



Check for updates

Gaseous elemental mercury (GEM) concentrations in the Arctic exhibit a distinct rebound during the summer months, with notable spatiotemporal variations observed in this phenomenon; however, the underlying mechanisms remain poorly understood. On the basis of targeted cruise observations from the Bering Strait to the North Pole, this study captured the summertime GEM rebound in the Pacific sector of the Arctic Ocean. Moreover, we identified synchronous increases in dissolved gaseous mercury (DGM) concentrations during the GEM rebound in the Marginal Ice Zone (MIZ). Combined with Generalized Additive Model (GAM) simulations, we confirm that oceanic mercury emissions from the MIZ contribute to this phenomenon. We also show that the spatiotemporal variability of dissolved organic components associated with phytoplankton, along with local atmospheric convection triggered by sea-ice melting in the MIZ, plays a crucial role in the observed spatiotemporal differences in the GEM rebound. In the context of rapid Arctic warming, with expected increases in primary productivity and more frequent local convection, the air-sea exchange of mercury is likely to intensify, amplifying the summertime "mercury source" effect in the Arctic Ocean.

Mercury (Hg) is a global pollutant with significant neurotoxic effects. When emitted into the atmosphere, Hg can be transported over long distances through atmospheric circulation, leading to its deposition and bioaccumulation in both terrestrial and aquatic ecosystems. This poses a serious threat to the ecological environment and human health^{1,2}. The Arctic plays a critical role as a sink in the Hg cycle within the Northern Hemisphere. The latest Arctic Monitoring and Assessment Program (AMAP) Report (2021) indicates that people living near the Arctic Circle experience some of the highest levels of Hg exposure in the world^{3,4}. Additionally, certain wildlife in the Arctic are highly vulnerable to Hg exposure due to the bioaccumulation of Hg in Arctic food webs5.

The exchange of Hg between the ocean and the atmosphere significantly influences the Hg budget in the Arctic. According to AMAP (2021), atmospheric Hg deposition contributes ~65 Mg/a of Hg to the Arctic Ocean, far surpassing riverine (41 Mg/a) and coastal erosion (39 Mg/a) inputs³. A recent modeling study reported a similar atmospheric Hg deposition flux in the Arctic Ocean (70.4 Mg/a), with 39 Mg/a deposited to the open ocean, 27.4 Mg/a deposited to snow, and 4.0 Mg/a deposited to sea-ice. This confirms that atmospheric Hg deposition is the largest Hg source in the Arctic Ocean⁶. Furthermore, the open ocean and seasonal sea-ice melting in the Arctic Ocean lead to the Hg evasion flux of 24.9 Mg/a and 27.8 Mg/a into the atmosphere, respectively, much higher than anthropogenic Hg emissions (14 Mg/a) and biomass burning Hg emissions (8.8 Mg/a) in the Arctic⁷. Thus, understanding the Hg cycle at the air-sea interface and its driving mechanisms is crucial for more accurately assessing the ecological impact of Hg in the Arctic.

Atmospheric gaseous elemental mercury (GEM or Hg(0)) in the Arctic exhibits unique seasonality, characterized by a springtime

¹Institute of Polar Environment & Anhui Key Laboratory of Polar Environment and Emerging Pollutants, School of Earth and Space Sciences, University of Science and Technology of China, Hefei, Anhui 230026, China. 2Univ. Grenoble Alpes, CNRS, INRAE, IRD, Grenoble INP, IGE, 38000 Grenoble, France. e-mail: yfg66@ustc.edu.cn; zgxie@ustc.edu.cn

minimum due to atmospheric mercury depletion events (AMDEs), followed by a noticeable summertime GEM rebound that can exceed Northern Hemisphere background concentrations $(1.58 \pm 0.31 \text{ ng/m}^3)^8$. Earlier studies proposed several potential mechanisms for this summertime GEM rebound, including long-range transport of anthropogenic Hg⁹, re-emission of Hg deposited on sea-ice and snowpacks during AMDEs, and oceanic Hg evasion from terrestrial Hg inputs (such as rivers and coastal erosion) around the Arctic Circle¹⁰⁻¹². A subsequent isotopic study suggested that the enhanced summertime GEM concentrations were primarily due to re-emissions from the Arctic cryosphere, with a minor role from terrestrial Hg emissions¹³. Our recent GEM observations during the Multidisciplinary Drifting Observatory for Arctic Climate (MOSAiC) expedition revealed that elevated GEM concentrations in summer are not uniform across the Arctic Ocean but are predominantly found in the Marginal Ice Zone (MIZ). This phenomenon may be driven by (1) the high load of divalent Hg (Hg(II)) in the MIZ due to melting ice water input, (2) the high reduction capacity of Hg(II) in the MIZ facilitated by elevated phytoplankton biomass, and (3) increased sea-air exchange due to sea-ice melting¹⁴. These factors likely contribute to the summertime GEM rebound in the Arctic¹⁴. However, the simultaneous measurements of Hg(0) in the surface ocean of the MIZ, a key piece of evidence for this mechanism, remain lacking. Additionally, the summertime GEM rebound displays clear seasonality and spatiotemporal variation, often peaking from mid-July to early August, followed by a gradual decline and levelling off after mid-August¹⁴. The reasons for these spatiotemporal variations are still unclear.

As part of the 13th Chinese National Arctic Research Expedition in 2023, we conducted large-scale, synchronized cruise observations of Hg(0) in both the atmosphere and surface ocean, from the Bering Strait to the North Pole (90°N) in the Arctic Ocean. This study aims to address these unresolved questions, contributing to a better understanding of oceanic Hg emissions in the Arctic MIZ and the atmospheric Hg cycle mechanisms in the Arctic marine boundary layer.

Results and discussion

Summertime GEM rebound in the Pacific sector of the Arctic Ocean

Regarding temporal variation, the GEM observations indicated significant concentration fluctuations from late July to mid-August, with several concentration peaks. The highest recorded concentration reached 2.08 ng/m³ in late July (Fig. 1a). We identified three distinct episodes of substantial GEM rebounds during this period, characterized by: (1) sustained increases in GEM concentrations with temporal thresholds (initial/terminal concentrations) exceeding the cruise's mean value (1.28 ± 0.20 ng/m³), and (2) peak magnitudes surpassing the Northern Hemisphere background reference level (1.58 ± 0.31 ng/ m³)8. These episodes are defined as the Arctic summertime "GEM rebound" phenomenon in this study (gray shaded areas in Fig. 1a, with episode 1 occurring from UTC 2023/7/28 0:00 to 2023/8/1 0:00; episode 2 occurring from UTC 2023/8/3 20:00 to 2023/8/6 18:00; and episode 3 occurring from UTC 2023/8/13 0:00 to 2023/8/15 0:00). In late summertime (mid-August to mid-September), the GEM concentrations stabilized and gradually decreased.

In terms of spatial distribution, the GEM rebound was primarily observed in the Chukchi Sea, where concentrations were notably higher than those in the Bering Strait, despite the latter being close to land and estuaries (Fig. 1b). This is consistent with the latitudinal distribution of GEM: both the mean and median concentrations of GEM in the 75–80°N area, where the Chukchi Sea is located, were higher than in other latitudinal regions of the Arctic Ocean (Fig. 1c). In contrast, GEM concentrations in the high-latitude Arctic Ocean (78–90°N) were relatively low, with minimal spatial variability.

The observations from the Pacific sector of the Arctic Ocean in this study, when combined with previous data from the Atlantic sector¹⁴, suggest that the summertime GEM rebound is widespread across the Arctic Ocean.

Sources of summertime GEM rebound

We explored the sources of the summertime GEM rebound in the Pacific sector of the Arctic Ocean. There was no positive correlation observed between NO_x and GEM concentrations (Fig. S1). NO_x levels were low during the GEM rebound at the end of July, whereas significant increases in NO_x coincided with a stable, low concentration trend of GEM after mid-August. Additionally, the Generalized Additive Model (GAM) simulation indicated that NO_x had a minimal contribution (4%) to GEM variability (Table 1), suggesting that anthropogenic sources, such as ship emissions, had little influence on the GEM rebound observed in this study (Fig. S1).

The fraction of the 168-h backward trajectories' transport time in marine areas (FRocean) was generally near 100% during the summertime GEM rebound (yellow shaded area in Fig. 2a). Statistical analysis of GEM and FRocean revealed that average FRocean levels were higher when GEM concentrations were elevated (GEM >1.6 ng/m³, t-test with p < 0.01), with the highest GEM concentration range (GEM >1.8 ng/m³) corresponding to the maximum FRocean average (0.998 ± 0.004, Fig. 2b). Furthermore, the GAM results indicated that the open-water fraction (Openwater, used as a proxy for oceanic emissions) had the greatest contribution (29%) to GEM variability (Table 1). These findings suggest that the GEM rebound in the Pacific sector of the Arctic Ocean was primarily driven by marine Hg emissions, rather than ship-based or land-based anthropogenic emissions and their regional transport.

PSCF (potential source contribution function) analysis was further applied to identify the potential source regions of GEM in the Arctic Ocean. High WPSCF (weighted potential source contribution function) values in the Pacific sector were primarily concentrated in the marginal ice zone (MIZ) of the Chukchi Sea, indicating elevated marine Hg emissions in this area. In contrast, both the open ocean regions of the outer Arctic Ocean and the pack ice zones in the high-latitude Arctic presented low WPSCF values (Fig. 3). The partial response curve of the GAM for Openwater is also consistent with the aforementioned phenomena: high concentrations of GEM correspond to an Openwater range of ~0.3–0.6, indicative of the environment of the marginal ice zone (Fig. S2a). These findings align with our previous observations in the Atlantic sector of the Arctic Ocean¹⁴, suggesting that high Hg emissions in the MIZ are a widespread phenomenon across both the Atlantic and Pacific sectors, serving as a key driver for the Arctic summertime Hg peak across the entire Arctic Ocean.

Characteristics of marine dissolved gaseous mercury during the summertime GEM rebound

To directly observe the source strength of oceanic mercury emissions from the MIZ during the summertime GEM rebound in the Arctic Ocean, synchronous measurements of marine dissolved gaseous mercury (DGM or Hg(0)) are essential. We aligned the observed DGM data with the original-resolution (5-min) GEM observations throughout the entire cruise based on their data point generation times, allowing us to comprehensively characterize the variability in marine Hg(0) concentrations during the GEM rebound periods. The results show clear synchronous increases in DGM concentrations during the GEM rebound in the MIZ (Fig. S3). We further averaged the GEM data to the temporal resolution of the DGM data and aligned them through observation times, and the results reveal a consistency in their variation trends with a significant positive correlation between DGM and GEM ($R^2 = 0.28$, P < 0.001) (Fig. 4). It should be noted that spatial heterogeneity may exist in the accumulation-release dynamics of DGM across different sampling locations. Additionally, meteorological conditions can also influence the accumulation and diffusion of GEM, all of which would collectively affect the correlation between DGM and GEM in this study. The observed synchronous increasing trends and

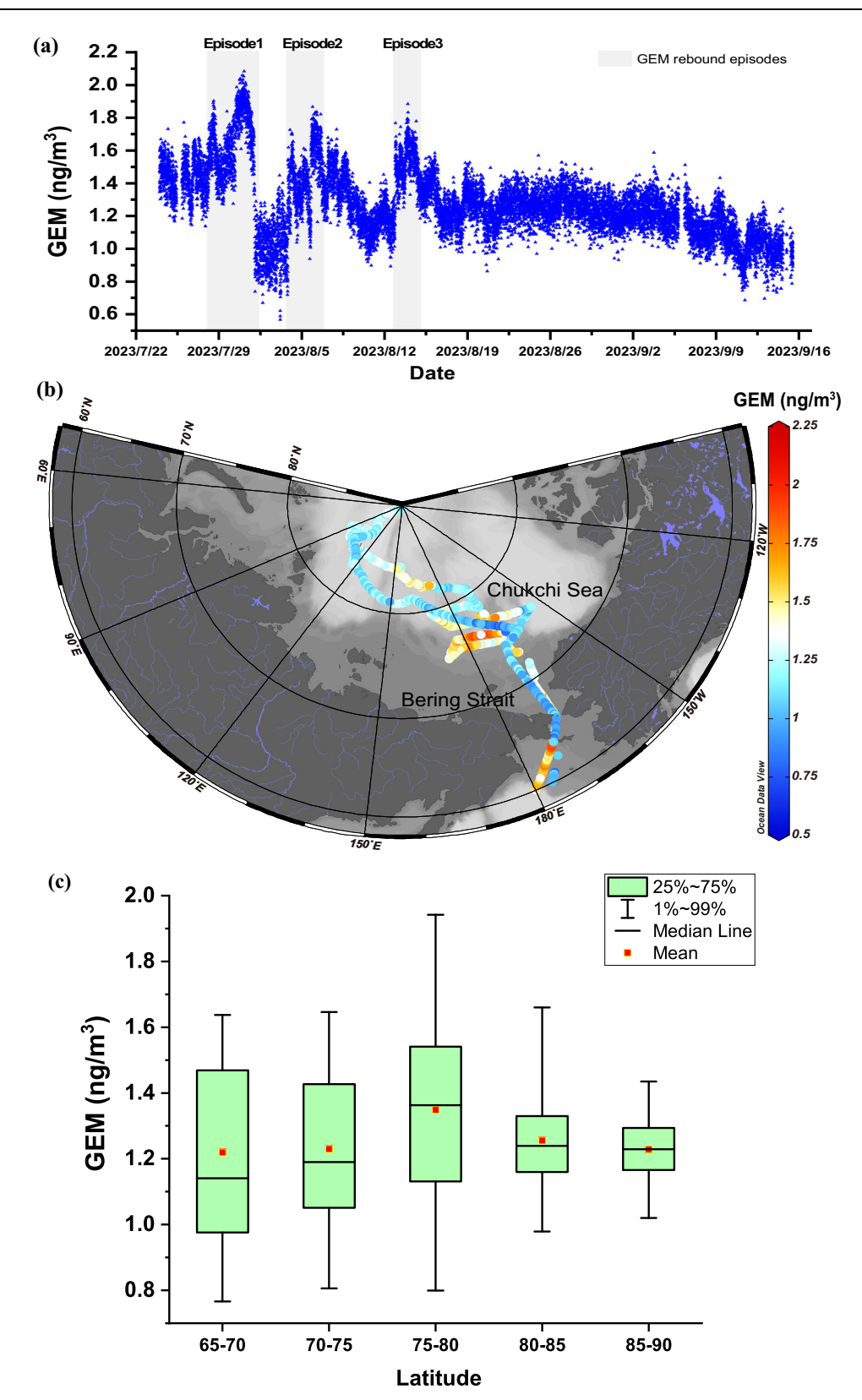


Fig. 1 | Time series and spatial distribution of observed gaseous elemental mercury (GEM) concentrations during this cruise. a Time series of gaseous elemental mercury (GEM) throughout the entire cruise, with gray shaded areas indicating the Arctic summertime GEM rebound episodes observed in this study;

b spatial distributions of GEM during the entire cruise; and **c** latitudinal variation in GEM throughout the cruise in the Pacific Ocean sector of the Arctic Ocean. The map was created with the scientific visualization software Ocean Data View 37 . Source data are provided as a Source Data file.

Table 1 | Relative importance of each predictor from Generalized Additive Model (GAM) results, including the openwater fraction (Openwater) during the cruise observations, NO_x mixing ratios, chromophoric dissolved organic matter (CDOM), wind speed (WS), air temperature (Temp), solar radiation (RD), and latent heat flux (EFLUX), along with their respective identifications and contributions

| Predictors | p values | Contributions | Identifications |
|---------------------|----------|---------------|-------------------------------|
| s(CDOM) | <2E-16 | 24% | Marine biochemical conditions |
| s(Openwater) | <2E-16 | 29% | Local oceanic emissions |
| s(WS) | 2.83E-06 | 7% | Meteorological conditions |
| s(Temp) | <2E-16 | 10% | _ |
| s(RD) | 2.53E-05 | 7% | _ |
| s(EFLUX) | <2E-16 | 19% | _ |
| s(NO _x) | 0.0231 | 4% | Anthropogenic emissions |

statistically significant correlation between the DGM and GEM during the GEM rebound period further provide evidence supporting the hypothesis that the Arctic Ocean GEM rebound is predominantly driven by Hg emissions from the MIZ.

The maximum DGM concentration observed during the GEM rebound reached 87 pg/L (i.e., 433 fM/L). This concentration is lower than the previously measured maximum instantaneous DGM concentrations under contiguous ice (e.g., 544 fM/L in ref. 15 and 670 fM/L in ref. 16), suggesting that DGM is likely released into the atmosphere following sea-ice melting. Additionally, the DGM saturation during the entire cruise ranged from 0.97 to 4.47, with an average of 2.40 ± 0.98 . A relatively high average saturation (2.79 \pm 0.87) was observed during the GEM rebound in the MIZ (Fig. S4), indicating high supersaturation (greater than 1) and high Hg evasion potential.

The calculated real-time air–sea exchange fluxes of Hg ranged from -0.043 to $6.88\, ng\cdot m^{-2}\cdot h^{-1}$. The average Hg(0) flux during the GEM rebound in the MIZ $(1.52\pm1.64\, ng\cdot m^{-2}\cdot h^{-1})$ was not only higher than the overall average for the entire cruise $(1.09\pm1.42\, ng\cdot m^{-2}\cdot h^{-1})$, but also exceeded previously reported flux levels in the open sea of the Arctic Ocean (ranging from $0.4\pm2.8\, ng\cdot m^{-2}\cdot h^{-1}$ to $0.7\pm0.26\, ng\cdot m^{-2}\cdot h^{-1})^{15.17}$. This suggests that the Arctic MIZ serves as a significant source of Hg to the atmosphere.

In summary, on the basis of the synchronous observation of GEM and DGM in the Pacific sector of the Arctic Ocean, this study further confirms that Hg emission from the MIZ is a crucial source of atmospheric Hg in the Arctic Ocean. It provides direct observational evidence supporting the mechanism by which high Hg emissions from the MIZ drive the summertime Hg rebound in the Arctic. This conclusion is also supported by the modeling results from ref. 18, which showed that oceanic evasion is the dominant source of the summer GEM rebound, particularly driven by seawater Hg(0) evasion facilitated by seasonal ice melt¹⁸. In ref. 18, both simulated atmospheric and seawater Hg(0) concentrations in the Arctic Ocean increased from the open ocean to the boundary between MIZ and perennial ice zone (PIZ).

Factors influencing the spatiotemporal variability of summertime GEM rebound

DiMento et al.¹⁵ conducted simultaneous observations of DGM and GEM in the Pacific sector of the Arctic Ocean from August to mid-October. Their study found that high DGM concentrations were primarily detected in the contiguous ice region north of 80°N¹5. Although both ref. 15 and this study observed similar sea-ice gradients in the MIZ –ranging from ice-free waters to areas with over 80% ice coverage – DGM concentrations in the Chukchi Sea MIZ were notably lower in ref. 15, and no distinct GEM rebound was observed in that region¹5.

Additionally, the Hg emission flux reported by ref. 15 in the MIZ was -3 ± 5 pmol·m⁻²·h⁻¹, with a surface seawater Hg saturation of

 0.39 ± 0.46 , indicating that the MIZ functioned as a Hg sink rather than a source at that time. A key difference between the two studies is the observation period: DiMento et al. ¹⁵ conducted their measurements in the MIZ ~20 days later than those in this study.

Similarly, ref. 14 observed a summertime GEM peak (2.99 ng/m³) in the MIZ during mid-July, nearly two weeks earlier and significantly higher than the maximum GEM concentration recorded in the MIZ in this study (2.08 ng/m³). However, after August, their observations showed continued GEM elevations, although with a much weaker rebound effect (<2 ng/m³), which aligns with the trends observed in this study during the same period.

These findings suggest a clear seasonal pattern in the oceandriven summertime GEM rebound in the MIZ, with the most pronounced effect occurring in July. As the season progresses into August, the process gradually weakens and eventually fades over time. The key question that arises is: What mechanisms drive this distinct spatiotemporal variability?

Dissolved organic components associated with primary productivity in the MIZ

Previous observations have shown a significant positive correlation between GEM and Chla (chlorophyll a) in surface seawater¹⁴, in which both parameters exhibit clear seasonal trends, with the peak concentrations occurring around mid-July, followed by a steady decline after August¹⁴. This suggests that the spatiotemporal variability in the summertime GEM rebound across the Arctic Ocean is closely linked to the evolution of primary productivity in the MIZ.

To further investigate this relationship, we analysed the connections between GEM, Chla, and chromophoric dissolved organic matter (CDOM) concentrations. Our findings indicate that the summertime GEM rebound generally coincided with seasonal phytoplankton bloom events (represented by Chla) in the MIZ from late July to early August, aligning with the observations of ref. 14. Additionally, we observed a strong association between GEM rebound events and sharp increases in CDOM during this period (Fig. 5a). By late August, GEM, Chla, and CDOM levels all remained low, and the GEM rebound disappeared.

Statistical analysis of the entire cruise dataset further supports this connection. During phytoplankton bloom periods (Chla >1.8 μ mol/L), both mean and median GEM concentrations were significantly higher (t-test with p < 0.01, Fig. 5b). In addition, as the CDOM concentration increased, the mean and median GEM levels followed an elevating trend (Fig. 5c). GAM analysis revealed that CDOM contributed significantly to GEM variability (24%), second only to the Openwater variable (29%) (Table 1). The GAM partial response curve of CDOM reveals that with increasing CDOM levels, GEM concentrations initially rise and then stabilize (Fig. S2b), exhibiting an overall positive correlation between the two variables, a pattern similar to that shown in Fig. 5c. These findings highlight the crucial role of dissolved organic components related to primary productivity in driving the Arctic summertime GEM rebound in the MIZ.

Moreover, the peak hourly-averaged GEM concentrations observed during the three GEM rebound events in this study corresponded well with peaks in solar radiation, with significant positive linear correlations between GEM and solar radiation across all events (Fig. S5). Laboratory studies have previously suggested that dissolved organic chromophores derived from phytoplankton exudates can enhance Hg(II) photoreduction, leading to increased DGM production in aquatic environments^{1,19,20}. On the basis of these observations, we conclude that the seasonal dynamics of dissolved organic components associated with phytoplankton activity in the MIZ play a key role in the spatiotemporal variations in the summertime GEM rebound in the Arctic Ocean, primarily by facilitating the photochemical reduction of Hg(II).

In addition to GEM, DGM concentrations in surface seawater also exhibited peak values in the MIZ, coinciding with increases in CDOM

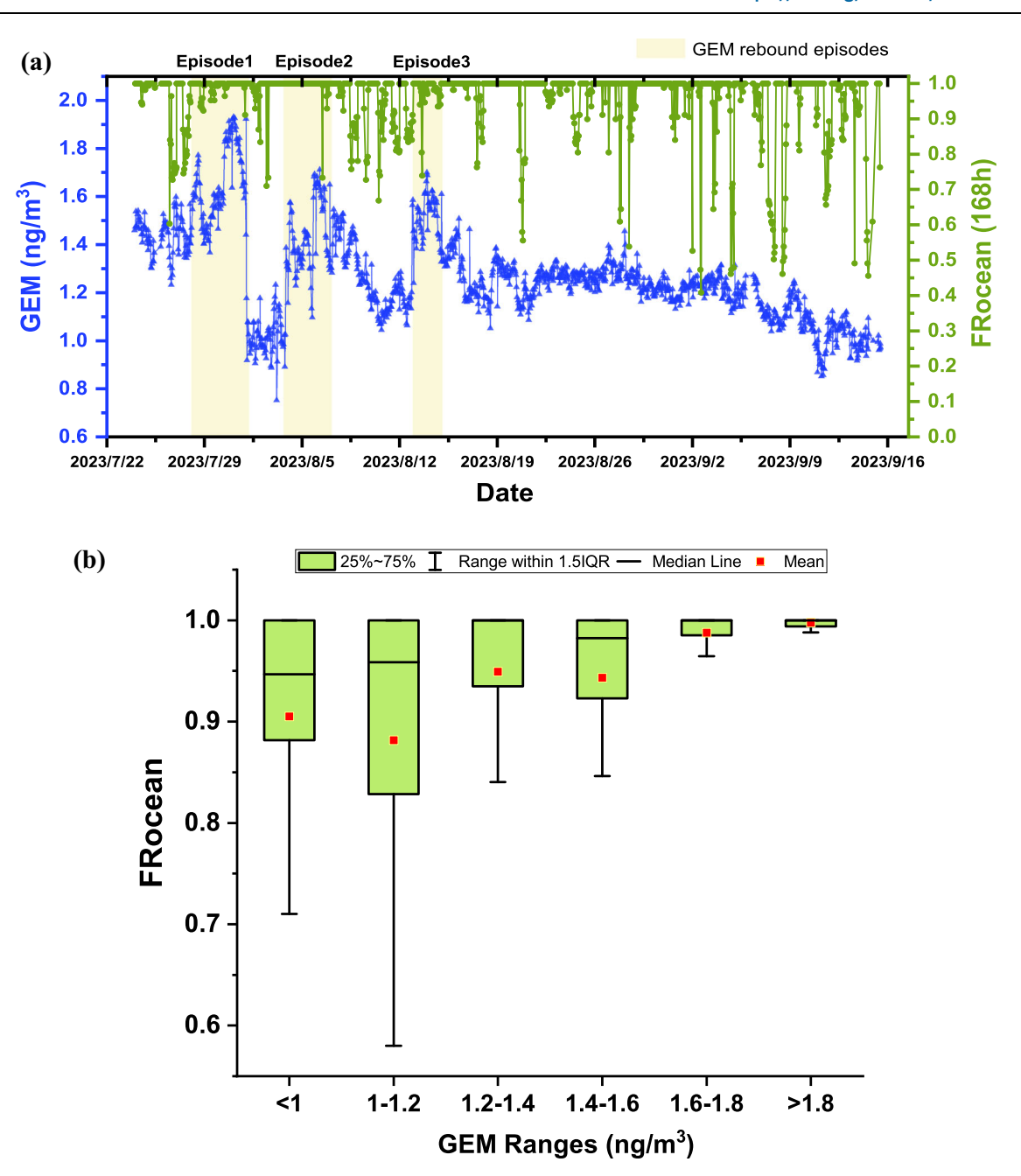


Fig. 2 | Time series of the fraction of the 168-h backward trajectory transport time spent in marine areas (FRocean) and statistical relationship between FRocean and gaseous elemental mercury (GEM). a Time series of hourly-averaged gaseous elemental mercury (GEM) concentrations and the fraction of the 168-h backward trajectory transport time spent in marine areas (FRocean)

throughout the entire cruise. The yellow shaded areas indicate the Arctic summertime GEM rebound episodes observed in this study; **b** Statistical distribution of FRocean in different GEM concentration ranges. Source data are provided as a Source Data file.

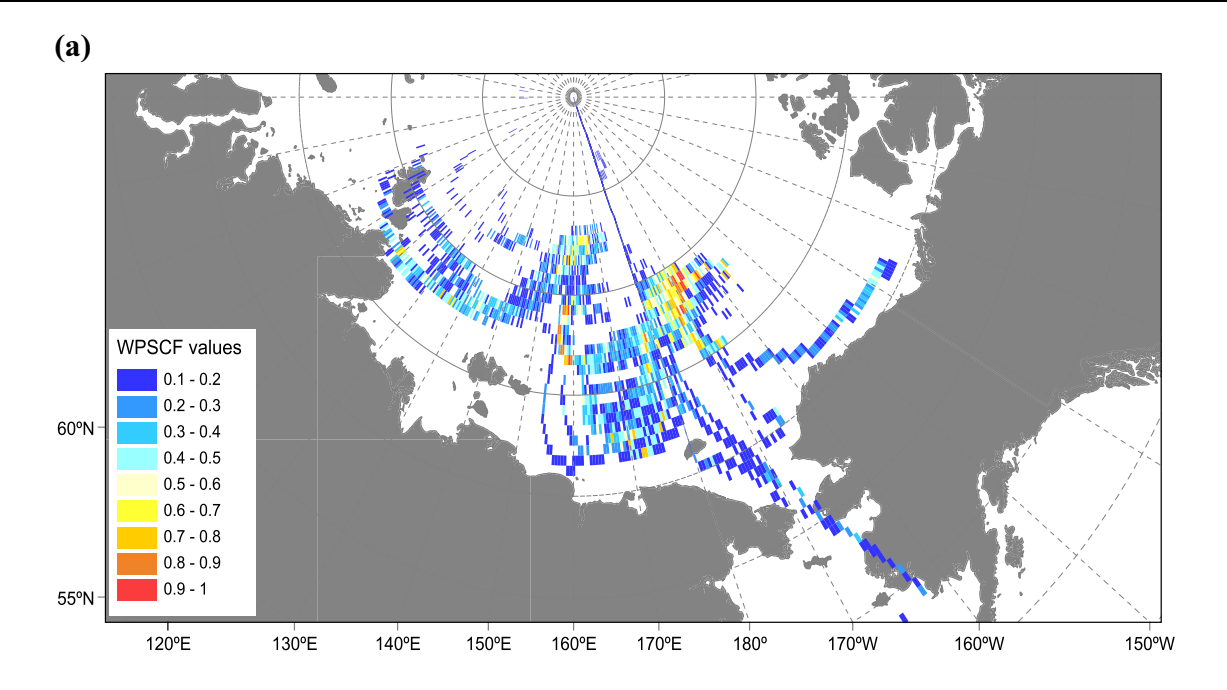
and Chla. Furthermore, the increase in DGM was closely linked to increased solar radiation (Fig. 5d). These covariation patterns among DGM, CDOM, Chla, and solar radiation further support the hypothesis that phytoplankton blooms in the MIZ enhance Hg(II) photoreduction at the sea surface, contributing to increased GEM emissions.

Building on these observations, this study further emphasizes the key role of increased primary productivity in the Arctic MIZ in driving the summertime GEM rebound, a phenomenon observed in both the Atlantic and Pacific sectors of the Arctic Ocean. The prominence of this process in the Arctic MIZ may be attributed to the shallow marine mixing layer formed by sea-ice melting. This shallow layer restricts the downward transport of Hg and dissolved organic matter, keeping them concentrated near the surface, where photoreduction and

subsequent re-emission of Hg are enhanced²¹. We propose that the temporal and spatial variability of dissolved organic components associated with algal blooms in the MIZ, combined with variations in solar radiation, are key factors contributing to the significant spatiotemporal differences observed in the summertime GEM rebound across the Arctic Ocean.

Meteorological processes at the ice-water-air interface

In addition to changes in primary productivity, sea-ice dynamics are among the most prominent seasonal characteristics of the Arctic Ocean. In addition to introducing deposited Hg(II) from melting ice, meteorological processes at the ice–water–air interface, which exhibit high spatial heterogeneity, also play a crucial role in regulating air–sea



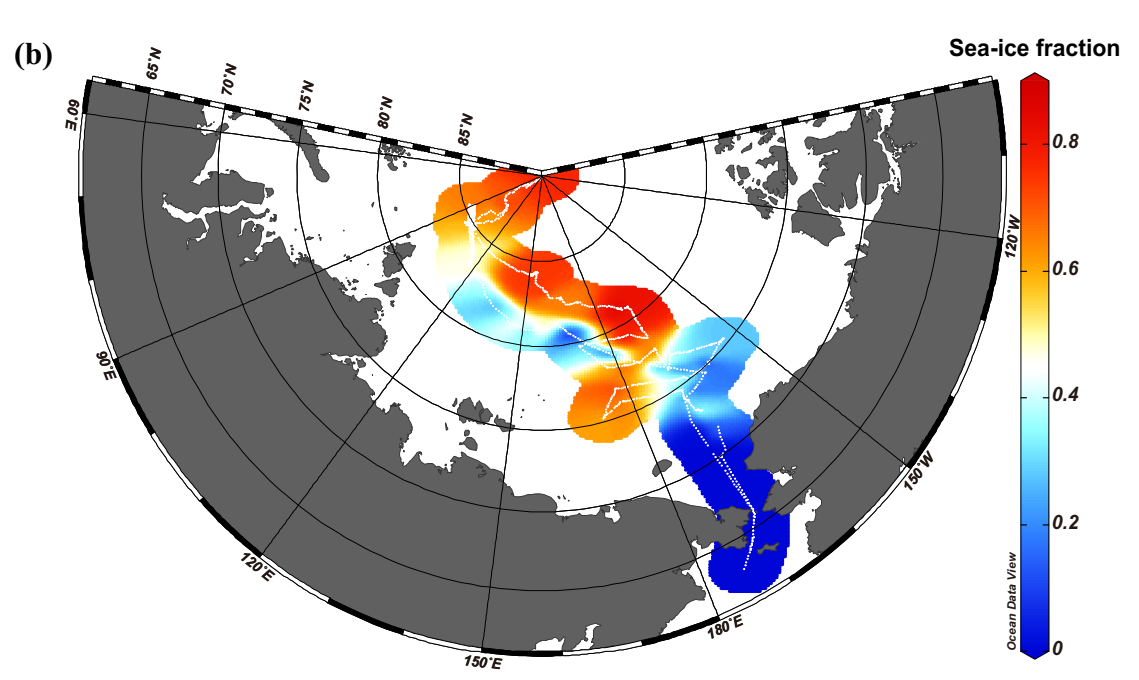


Fig. 3 | Potential source contribution function (PSCF) analysis of gaseous elemental mercury (GEM) and spatial distribution of the sea-ice fraction during this cruise. a Results of the weighted potential source contribution function (WPSCF) analysis for gaseous elemental mercury (GEM) over the entire observation

period, and **b** spatial distribution of the sea ice fraction throughout the observation period. The map was created with the scientific visualization software MeteoInfo (**a**), and Ocean Data View³⁷ (**b**), respectively. Source data are provided as a Source Data file.

exchange. Moore et al.²² reported that lead-initiated shallow convection in the stable Arctic boundary layer can mix GEM from undepleted air masses aloft, leading to rapid GEM recovery during atmospheric mercury depletion events (AMDEs) in spring. This highlights the important role of local atmospheric convection, driven by sea-ice dynamics, on the atmospheric Hg cycle.

In this study, we observed that air–sea temperature differences (Air_sea_Temp) remained generally stable during the late-July GEM rebound events (Fig. S6), but closely followed GEM fluctuations throughout August (Fig. 6a). The two GEM rebound episodes in August coincided with increased in Air_sea_Temp, showing a significant linear correlation in August ($R^2 = 0.3$, P < 0.001, Fig. 6b). This suggests that

local atmospheric convection, facilitated by increasing air–sea temperature differences in open water in the sea–ice region, likely enhanced oceanic Hg emissions during this period.

To further verify this hypothesis, we examined evaporation from turbulence (EVAP) and sea-air latent heat flux (EFLUX)—both key indicators of atmospheric turbulence at the sea-air interface. In late July, EFLUX and EVAP variations showed no clear correlation with GEM, implying minimal impact from local convection on the July GEM rebound event (Fig. S6). However, in August, notable increases in EFLUX and EVAP corresponded well with GEM rebounds (Fig. 6c), with a significant positive exponential correlation between EFLUX and GEM (R^2 = 0.33, P < 0.001, Fig. 6d). GAM analysis across the entire cruise

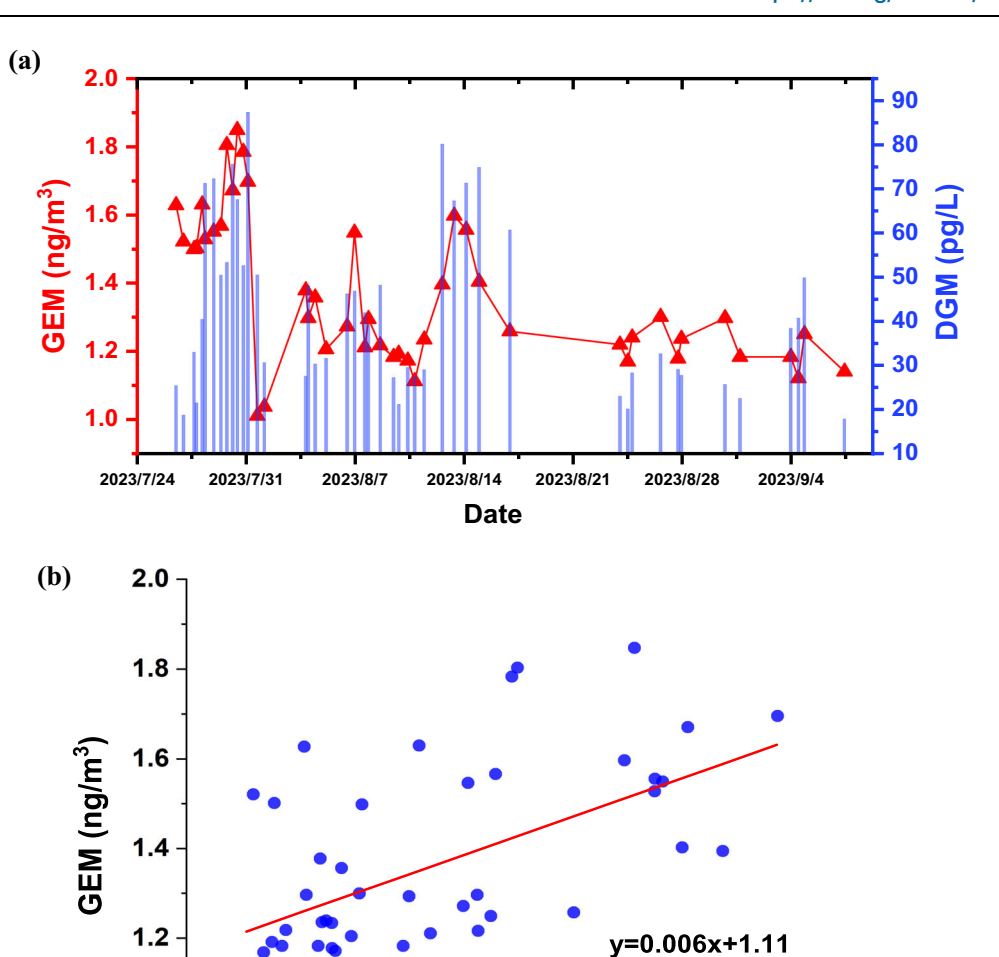


Fig. 4 | Time series and relationship between gaseous elemental mercury (GEM) and dissolved gaseous mercury (DGM). a Time series of gaseous elemental mercury (GEM) and dissolved gaseous mercury (DGM) during the whole cruise. The

1.0

10

20

30

40

50

DGM (pg/L)

60

70

temporal resolution of GEM was matched to DGM here according to observation frequency and temporal resolution of DGM; **b** correlation between GEM and DGM during the whole cruise. Source data are provided as a Source Data file.

90

R²=0.28 P<0.001

80

further showed that EFLUX contributed 19% to GEM variability, ranking third after Openwater (29%) and CDOM (24%) (Table 1). Additionally, the GAM partial response curve of EFLUX demonstrates a pattern analogous to that observed in Fig. 6d: when EFLUX exceeds 5 W/m², GEM concentrations exhibit an overall upward trend with increasing EFLUX values (Fig. S2c). These findings indicate that local atmospheric convection had a substantial influence on most of the observed GEM rebound events in this study.

Integrating sea-ice data, we observed that elevated levels of GEM and EFLUX generally corresponded to a moderate sea-ice fraction (0.5 ~ 0.8), whereas both lower GEM and EFLUX levels were associated with either dense ice cover (sea-ice fraction >0.8) or melting ice area (sea-ice fraction <0.5) (Fig. 6d). These findings suggest that the influence of local convection on oceanic Hg emissions in the Arctic Ocean is closely linked to the extent of sea-ice melt. When sea-ice coverage is extensive (>80%), the consolidated ice inhibits the release of oceanic Hg¹⁵. However, as melting progresses and open water expands, the shoaling of the mixing layer caused by meltwater facilitates the accumulation of Hg previously trapped in sea-ice at the sea surface. Additionally, the enhanced temperature gradient between the open water

and air immediately after melting promoted local atmospheric convection and evaporation, further stimulating the release of oceanic Hg into the atmosphere. Once sea ice has completely melted, the input of Hg from ice diminishes, along with its subsequent re-emission²³.

These findings indicate that meteorological processes at the ice—water—air interface, driven by dynamic and thermodynamic sea-ice changes, would not only influence AMDEs but also modulate oceanic Hg emissions during the summer. This represents another key mechanism contributing to the spatiotemporal variations in the summertime GEM rebound within the Arctic MIZ. A conceptual summary of the primary processes involving dissolved organic matter associated with primary productivity and local convection, which drive the pronounced spatiotemporal differences in Arctic summertime GEM rebound, is presented in Fig. 7.

Building on the findings of ref. 14, we observed the summertime GEM rebound phenomenon once again in the North Pacific sector of the Arctic Ocean, indicating that this phenomenon may be widespread throughout the Arctic. Our study revealed simultaneous increases in Hg(0) concentrations in surface seawater within the MIZ during the summertime GEM rebound, providing key evidence that oceanic Hg

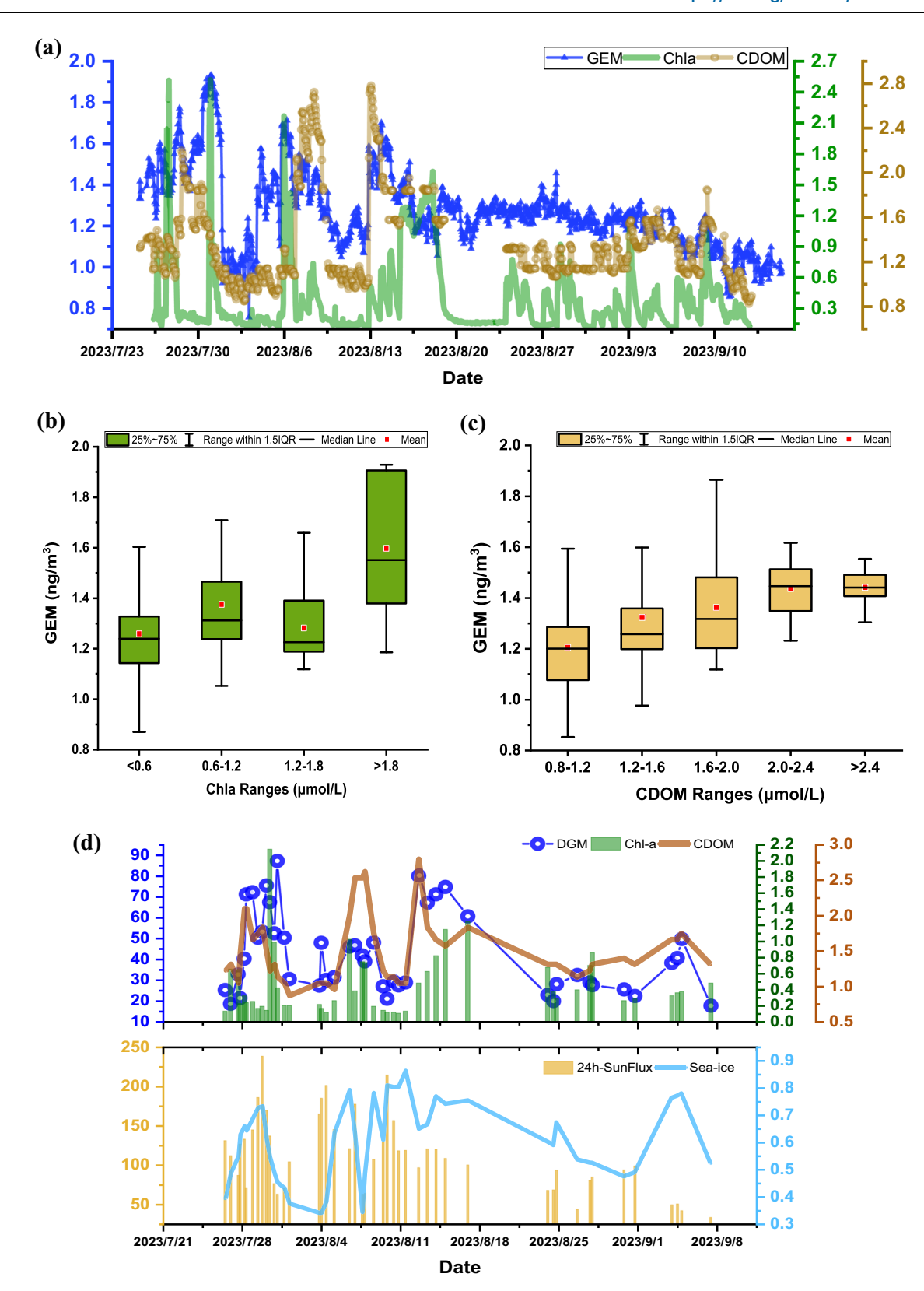


Fig. 5 | Time series and statistical information of gaseous elemental mercury (GEM) and several environmental parameters. a Time series of hourly-averaged gaseous elemental mercury (GEM), chlorophyll a (Chla, μ mol/L) and chromophoric dissolved organic matter (CDOM, μ mol/L) throughout the cruise; statistical distribution of GEM concentrations across different **b** Chla and **c** chromophoric

dissolved organic matter (CDOM) concentration ranges. **d** Covariation trends of dissolved gaseous mercury (DGM), Chla, CDOM, 24-h average solar radiation (24-h-SunFlux) and sea-ice fraction (sea-ice). Source data are provided as a Source Data file.

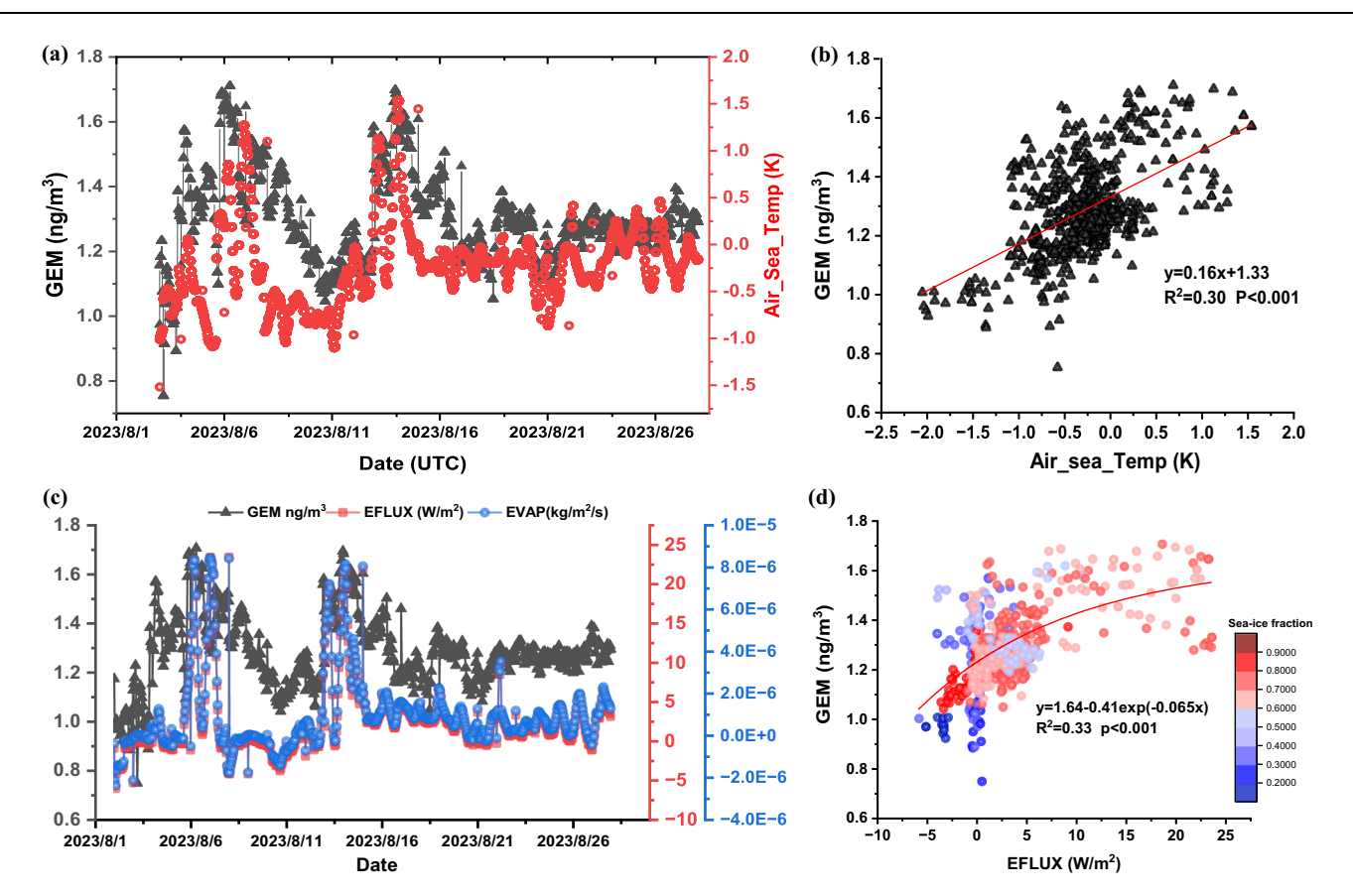


Fig. 6 | Variation characteristics and their relationship between gaseous elemental mercury (GEM) and several meteorological parameters. a Covariation of hourly-averaged gaseous elemental mercury (GEM) with air–sea temperature difference (Air_sea_Temp) in August; b correlation between GEM and Air_sea_Temp in

August; **c** Covariation of hourly-averaged GEM with evaporation from turbulence (EVAP) and latent heat flux (EFLUX) in August; and **d** correlation between GEM and EFLUX in August. The color bar indicates the corresponding sea-ice fractions. Source data are provided as a Source Data file.

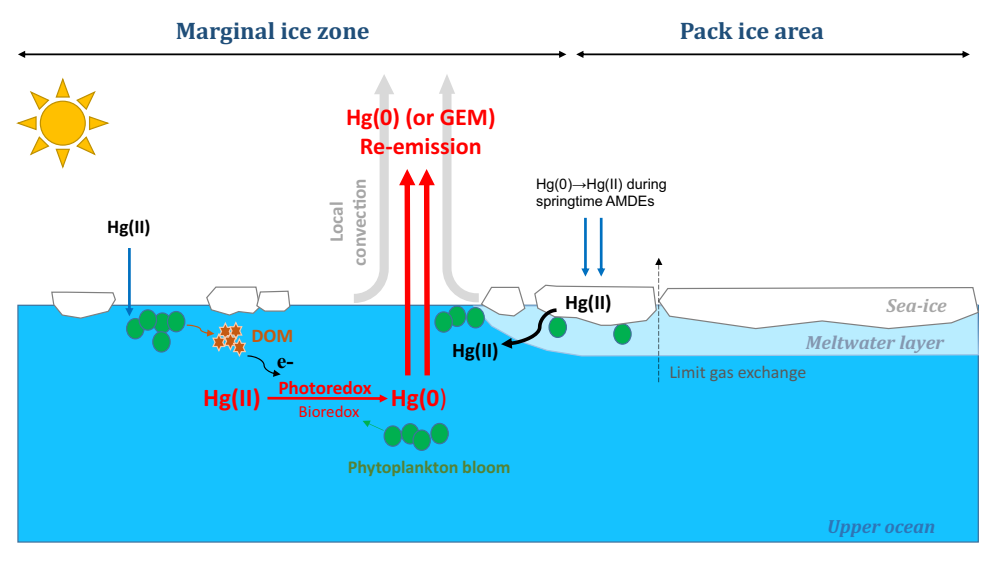


Fig. 7 | Schematic diagram illustrating the key processes contributing to the pronounced spatiotemporal differences in the summertime gaseous elemental mercury (GEM) rebound phenomenon in the Arctic Ocean. During early summer (July to early August), extensive phytoplankton blooms in marginal ice zones (MIZ) release large amounts of dissolved organic matter (DOM), which facilitates the

photochemical (and potentially biological) reduction of Hg(II). Additionally, local convection driven by air–sea temperature gradients following sea-ice melt further enhances the emission of Hg(0) into the atmosphere, thereby driving the summertime GEM rebound.

emissions from the MIZ play a dominant role in driving this phenomenon. This finding highlights a seasonal shift in the role of the Arctic Ocean, transitioning from a "Hg sink" in spring to a "Hg source" in summer.

In conjunction with ref. 14 and previous experimental studies, our results emphasize the role of marine phytoplankton in facilitating the re-emission of marine Hg in the MIZ, potentially reducing the Hg exposure levels of marine biota during the summer months. Future research should focus on elucidating the detailed mechanisms behind this process, including identifying the dominant phytoplankton species and organic components involved. Given that phytoplankton can also contribute to methylmercury formation in the subsurface ocean by creating anaerobic microenvironments^{24,25}, which could increase Hg exposure for marine organisms, the broader role of phytoplankton in the marine Hg cycle and its complex ecological effects require further investigation.

Additionally, this study highlights the role of local convection driven by sea-ice melting in enhancing the "Hg source" effect in the Arctic Ocean during summer. This effect differs from its impact in spring when local convection may resupply GEM from higher altitudes into the surface atmosphere, allowing it to participate in renewed halogen-initiated depletion and reinforcing the "Hg sink" effect in the Arctic Ocean²². Future studies should clarify the significance of these processes for polar atmospheric chemistry.

In the context of rapid Arctic warming, with an expected extension of the phytoplankton growing season and more frequent local convection due to pronounced seasonal sea ice changes^{26–28}, the exchange of Hg between the Arctic Ocean and the atmosphere is likely to intensify. This intensification will amplify the seasonal variability in the Arctic Hg budget, strengthening the "Hg sink" effect in spring and the "Hg source" effect in summer. The ecological consequences of these seasonal shifts warrant further investigation.

Methods

Study site

As part of the 13th Chinese National Arctic Research Expedition (CHINARE), which focused on the Arctic climate and ecosystem, a large-scale, multidisciplinary observational cruise was conducted in the Pacific sector of the Arctic Ocean. The expedition route began at the Bering Strait, passed through the Chukchi Sea and the Guck mid-ocean ridge, and extended to the North Pole (90°N), covering a latitudinal range from 60°N to 90°N and a longitudinal range from 90°E to 150°W. The cruise took place from July 24 to September 15, 2023, and traversed diverse hydrological environments, including open waters, marginal ice zones, and ice-covered regions. The cruise track is shown in Fig. 1.

Experimental methods

Atmospheric GEM was automatically measured using a Tekran[™] 2537B Hg analyser based on cold vapor atomic fluorescence spectroscopy (CVAFS), with a temporal resolution of 5 min per data point. The air inlet of the Hg analyser was positioned at the front of the research vessel Xuelong 2, -30 m above the sea surface, to minimize contamination from the ship's exhaust plume. GEM was alternately collected on two gold cartridges at a constant flow rate of 0.7 L·min⁻¹, then thermally desorbed at 550 °C and detected by CVAFS.

To remove moisture and coarse particles, two soda lime tubes and two 0.45-µm Teflon filters were installed at the analyser's inlet. Daily calibration was performed using an internal Hg permeation source built into the analyser. In addition, external calibration was conducted before and after the cruise by manually injecting a known GEM mass via a TekranTM 2505 unit. Both internal and external calibration procedures achieved an accuracy of 96%. The detection limit (DL) of the analyser for GEM was less than 0.10 ng·m⁻³.

Dissolved gaseous mercury (DGM) in seawater was measured using a purge-trap-detect method adapted from refs. 29,30. A

specified volume of surface seawater was automatically drawn from the onboard seawater tap into a pre-conditioned Teflon bubble chamber via a Teflon tube. The seawater sample was purged with Hg-free air (produced by a TekranTM zero air generator) at a flow rate of $1 L \cdot min^{-1}$ for 1 h. The purged air stream was passed through a soda lime tube to remove moisture and then routed to another TekranTM 2537B analyser for Hg detection. The DL for DGM was 4.8 pg·L⁻¹, calculated as three times the standard deviation of the blank (1.3 ± 1.6 pg·L⁻¹, n = 17).

DGM observations depend on sea-ice conditions in the Arctic Ocean. When the sea-ice density was too high, the onboard seawater pump was turned off to prevent ice blockage in the sampling system. Therefore, DGM measurements were conducted only when open water was present within the sea-ice cover.

Hg sea-air flux calculation

The saturation of DGM in surface seawater and the sea-air flux of GEM were calculated via the thin-film gas exchange model³⁰⁻³³. Specifically, the saturation (S) were determined using the following equations:

$$S = DGM \times H'(T)/GEM$$
 (1)

where T is the surface seawater temperature (K), and H'(T) is the temperature-dependent Henry's law constant. H'(T) was calculated based on the method of ref. 34:

$$H'(T) = \exp(-2404.3/T + 6.29)$$
 (2)

The sea–air flux (F, ng·m $^{-2}\cdot h^{-1})$ was determined using the following equation:

$$F = K_W \times (DGM - GEM/H'(T))$$
 (3)

where K_w is the gas transfer velocity of Hg(0) at the water–air interface (in cm·h⁻¹). Kw was calculated based on ref. 31:

$$K_W = 0.31U_{10}^2 (S_{Hg}/600)^{-0.5}$$
 (4)

where S_{Hg} is the Schmidt number for Hg, derived from ref. 30, and U_{10} is the 10 m wind speed (m·s⁻¹).

Other ancillary data and analysis

Nitrogen oxides (NO_x) were continuously measured on an hourly basis using a Thermo FisherTM-42i chemiluminescence $NO-NO_2-NO_x$ analyser. Marine biogeochemical parameters, including chlorophyll a (Chla) and chromophoric dissolved organic matter (CDOM), were monitored using a WET LabsTM ECO-triplet fluorometer, which includes dedicated sensors for Chla and CDOM. The temperature of surface seawater was monitored using a Sea-birdTM SBE-38 Digital Oceanographic Thermometer. These measurements were conducted during the DGM observations, and the corresponding raw data were averaged hourly for subsequent analysis.

Hourly navigation parameters and selected meteorological variables, including wind speed and air temperature, were obtained from the shipboard monitoring systems. Additionally, hourly data, including sea-ice fraction, solar radiation (Radiation), air–sea temperature difference (Air_sea_Temp), evaporation due to turbulence (EVAP), and latent heat flux (EFLUX), were extracted from assimilated meteorological datasets provided by the Goddard Earth Observing System (GEOS) and the Modern-Era Retrospective Analysis for Research and Applications, Version 2 (MERRA-2), with a horizontal resolution of $2^{\circ} \times 2.5^{\circ}$.

The HYSPLIT transport and dispersion model developed by the NOAA-Air Resources Laboratory was used to generate 168-hour backward trajectories of air masses throughout the cruise. These trajectories enabled further statistical analyses of air mass origin,

including the calculation of the fraction of each 168-h trajectory's transport time spent over marine areas relative to the total transport time (FRocean). The model was driven by the meteorological data from the global data assimilation system (GDAS). One trajectory was generated per hour, resulting in a total of 1280 trajectories over the course of the cruise.

Evaluating the relative importance of various influencing factors In this study, we employed a generalized additive model (GAM) to assess the relative contribution of selected predictors to the observed variability in GEM concentrations. As a data-driven statistical framework, GAM accommodates nonlinear relationships between dependent and independent variables by incorporating flexible basis

functions. The model structure is defined as:

$$g(\mu) = f_1(x_1) + f_2(x_2) + \dots + f_n(x_n) + \varepsilon$$
 (5)

where xi (i = 1, 2, 3, ..., n) represents the predictor variables, fi denotes the smooth function applied to each predictor, μ is the expected value of the response variable, ϵ is the residual, and g is the link function. To optimize model performance, penalized cubic regression splines were adopted for fi, allowing adaptive selection of degrees of freedom to mitigate overfitting or underfitting. Given the Gaussian distribution of GEM values, the identity link function was paired with a Gaussian. All analyses were performed using the "mgcv" package in R.

We considered four categories of predictors, including the following parameters to evaluate their relative importance to GEM variation in this study:

- Oceanic emissions: indicated by the open-water fraction (Openwater) during the cruise observation;
- Anthropogenic emissions: indicated by the observed NO_x mixing ratios;
- Marine biochemical conditions: indicated by chromophoric dissolved organic matter (CDOM);
- (4) Meteorological factors: wind speed (WS), air temperature (Temp), solar radiation (RD) and latent heat flux (EFLUX). The corresponding results were displayed in Table 1.

Previous studies have indicated that the GAM demonstrates robust performance when the adjusted R^2 value exceeds $0.5^{35,36}$. In this study, the GAM analysis explains 52.9% of the variance in GEM concentrations, achieving a fitting R^2 of 0.53. This result underscores the model's capacity to effectively characterize GEM variability across the entire observational period, reflecting its strong applicability in this context (Fig. S7a).

We used the Akaike Information Criterion (AIC) to ensure the effectiveness of the predictors' selection. Proper parameter selection can be indicated by higher fitting R^2 values along with lower AIC values during the addition of each variable^{35,36}. The corresponding results indicate that they met the criterion of the AIC evaluation (Fig. S8d).

Model validation

Systematic evaluation of the GAM's performance was conducted through multiple validation techniques to ensure model reliability. A fivefold cross-validation approach was applied to assess predictive accuracy¹⁴. Under this method, the dataset was partitioned into five random subsets, with four subsets used for model fitting and the remaining subset reserved for validation in each iteration. This process was repeated five times, ensuring that all the subsets served as test data. The cross-validation results exhibited strong alignment between the simulated and observed values (slope = 0.97, $R^2 = 0.93$), confirming robust model performance (Fig. S7b).

To validate the assumptions of homogeneity, normality, and independence of residuals and ensure methodological rigor, three diagnostic analyses were performed^{35,36}: (1) quantile-quantile (Q-Q)

plot (comparing sample vs. theoretical quantiles); (2) residual scatterplots against linear predictors; and (3) residual histograms. The Q-Q plot revealed that GAM predictions closely matched theoretical quantiles, particularly near the mean concentration. Residual scatterplots demonstrated residuals clustered near zero with no discernible trend, indicating unbiased simulations. The residual histogram approximated a normal distribution, suggesting a random error structure and appropriate predictor selection. Collectively, these results underscore the validity of the model's assumption and the reliability of using the selected predictors to identify GEM sources and key influencing factors in this study (Fig. S8).

PSCF analysis

A potential source contribution function analysis (PSCF) was performed to identify the potential source regions of GEM in the Arctic Ocean during the observation period. A higher value of *WPSCFij* indicates a higher probability that a given region contributed to elevated GEM levels at the receptor site. PSCF analysis driven by GDAS meteorological data combines the measured hourly GEM concentrations with 72-h HYSPLIT backwards trajectories. The domain of the 72-h backward trajectories was divided into $0.5^{\circ} \times 0.5^{\circ}$ grid cells. The *PSCF* value for the ij_{th} cell was calculated as follows:

$$WPSCF_{ij} = \frac{M_{ij}}{N_{ii}} \times W_{ij} \tag{6}$$

in which *Mij* is the number of trajectory segment endpoints in a grid cell with a corresponding GEM concentration higher than its 90th percentile of the whole cruise, and *Nij* is the total number of trajectory segment endpoints in a grid cell. The empirical weight coefficient *Wij* was included in the calculation to reduce the uncertainties of grid cells with small *Nij* values, and its values can be found in the ref. 36.

Data availability

The GEM, DGM concentrations and the corresponding auxiliary data generated in this study are provided in the Source Data file and are available at figshare: (https://figshare.com/articles/dataset/Observed_GEM_and_DGM_data_in_the_Arctic_Ocean/28057997). Source data are provided with this paper.

Code availability

The R code of the generalized additive model (GAM) used in this study is available at: (https://figshare.com/articles/dataset/Observed_GEM_and_DGM_data_in_the_Arctic_Ocean/28057997). The PSCF method and the corresponding software used in this study can be accessed here: (http://www.meteothink.org/).

References

- Ariya, P. A. et al. Mercury physicochemical and biogeochemical transformation in the atmosphere and at atmospheric interfaces: a review and future directions. *Chem. Rev.* 115, 3760–3802 (2015).
- Driscoll, C. T., Mason, R. P., Chan, H. M., Jacob, D. J. & Pirrone, N. Mercury as a global pollutant: sources, pathways, and effects. *Environ. Sci. Technol.* 47, 4967–4983 (2013).
- AMAP. 2021 AMAP Mercury Assessment. Summary for Policymakers. (AMAP, 2021).
- Basu, N. et al. The impact of mercury contamination on human health in the Arctic: a state of the science review. Sci. Total Environ. 831, 154793 (2022).
- St. Louis, V. L. et al. Differences in mercury bioaccumulation between polar bears (*Ursus maritimus*) from the Canadian high- and sub-Arctic. *Environ. Sci. Technol.* 45, 5922–5928 (2011).
- Huang, S. et al. Modeling the mercury cycle in the sea ice environment: a buffer between the polar atmosphere and ocean. *Environ. Sci. Technol.* 57, 14589–14601 (2023).

- Dastoor, A. et al. Arctic mercury cycling. Nat. Rev. Earth Environ. 3, 270–286 (2022).
- Bencardino, M. et al. Patterns and trends of atmospheric mercury in the GMOS network: insights based on a decade of measurements. *Environ. Pollut.* 363, 125104 (2024).
- Durnford, D., Dastoor, A., Figueras-Nieto, D. & Ryjkov, A. Long range transport of mercury to the Arctic and across Canada. *Atmos. Chem. Phys.* 10, 6063–6086 (2010).
- Lindberg, S. E. et al. Dynamic oxidation of gaseous mercury in the Arctic troposphere at polar sunrise. *Environ. Sci. Technol.* 36, 1245–1256 (2002).
- Hirdman, D. et al. Transport of mercury in the Arctic atmosphere: evidence for a spring-time net sink and summer-time source. Geophys. Res. Lett. 36 (2009).
- Fisher, J. A. et al. Riverine source of Arctic Ocean mercury inferred from atmospheric observations. Nat. Geosci. 5, 499–504 (2012).
- Araujo, B. F. et al. Mercury isotope evidence for Arctic summertime re-emission of mercury from the cryosphere. *Nat. Commun.* 13, 4956 (2022).
- Yue, F. et al. The marginal ice zone as a dominant source region of atmospheric mercury during central Arctic summertime. *Nat. Commun.* 14, 4887 (2023).
- DiMento, B. P., Mason, R. P., Brooks, S. & Moore, C. The impact of sea ice on the air-sea exchange of mercury in the Arctic Ocean. *Deep* Sea Res. I Oceanogr. Res. Pap. 144, 28–38 (2019).
- Andersson, M. E., Sommar, J., Gårdfeldt, K. & Lindqvist, O. Enhanced concentrations of dissolved gaseous mercury in the surface waters of the Arctic Ocean. *Mar. Chem.* 110, 190–194 (2008).
- Kalinchuk, V. V., Lopatnikov, E. A., Astakhov, A. S., Ivanov, M. V. & Hu, L. Distribution of atmospheric gaseous elemental mercury (Hg(0)) from the Sea of Japan to the Arctic, and Hg(0) evasion fluxes in the Eastern Arctic seas: results from a joint Russian-Chinese cruise in fall 2018. Sci. Total Environ. 753, 142003 (2021).
- Huang, S. et al. Oceanic evasion fuels Arctic summertime rebound of atmospheric mercury and drives transport to Arctic terrestrial ecosystems. Nat. Commun. 16, 903 (2025).
- Lanzillotta, E. et al. Importance of the biogenic organic matter in photo-formation of dissolved gaseous mercury in a culture of the marine diatom Chaetoceros sp. Sci. Total Environ. 318, 211–221 (2004).
- Deng, L., Fu, D. & Deng, N. Photo-induced transformations of mercury(II) species in the presence of algae, *Chlorella vulgaris*. J. Hazard. Mater. 164, 798–805 (2009).
- Creamean, J. M. et al. Annual cycle observations of aerosols capable of ice formation in central Arctic clouds. *Nat. Commun.* 13, 3537 (2022).
- Moore, C. W. et al. Convective forcing of mercury and ozone in the Arctic boundary layer induced by leads in sea ice. *Nature* 506, 81–84 (2014).
- 23. Yue, F., Xie, Z., Yan, J., Zhang, Y. & Jiang, B. Spatial distribution of atmospheric mercury species in the Southern Ocean. *J. Geophys. Res.: Atmospheres* **126**, e2021JD034651 (2021).
- 24. Gallorini, A. & Loizeau, J. L. Mercury methylation in oxic aquatic macro-environments: a review. *J. Liminol.* **80** (2021).
- Heimbürger, L.-E. et al. Shallow methylmercury production in the marginal sea ice zone of the central Arctic Ocean. Sci. Rep. 5, 10318 (2015).
- Lewis, K. M., van Dijken, G. L. & Arrigo, K. R. Changes in phytoplankton concentration now drive increased Arctic Ocean primary production. Science 369, 198–202 (2020).
- 27. Jahn, A., Holland, M. M. & Kay, J. E. Projections of an ice-free Arctic Ocean. *Nat. Rev. Earth Environ.* **5**, 164–176 (2024).
- Arrigo, K. R., van Dijken, G. & Pabi, S. Impact of a shrinking Arctic ice cover on marine primary production. Geophys. Res. Lett. 35 (2008).

- 29. Fu, X. et al. Mercury in the marine boundary layer and seawater of the South China Sea: concentrations, sea/air flux, and implication for land outflow. *J. Geophys. Res. Atmos.* **115** (2010).
- 30. Wang, J., Xie, Z., Wang, F. & Kang, H. Gaseous elemental mercury in the marine boundary layer and air-sea flux in the Southern Ocean in austral summer. Sci. Total Environ. **603-604**, 510–518 (2017).
- Wanninkhof, R. Relationship between wind speed and gas exchange over the ocean. J. Geophys. Res. Oceans 97, 7373–7382 (1992).
- Andersson, M. E., Sommar, J., Gårdfeldt, K. & Jutterström, S. Air-sea exchange of volatile mercury in the North Atlantic Ocean. *Mar. Chem.* 125, 1–7 (2011).
- Yue, F., Xie, Z., Zhang, Y., Yan, J. & Zhao, S. Latitudinal distribution of gaseous elemental mercury in tropical Western Pacific: the role of the doldrums and the ITCZ. *Environ. Sci. Technol.* 56, 2968–2976 (2022).
- Andersson, M. E., Gårdfeldt, K., Wängberg, I. & Strömberg, D. Determination of Henry's law constant for elemental mercury. Chemosphere 73, 587–592 (2008).
- 35. Wu, Q. et al. Developing a statistical model to explain the observed decline of atmospheric mercury. *Atmos. Environ.* **243**, 117868 (2020).
- Zhang, L. et al. Quantifying the impacts of anthropogenic and natural perturbations on gaseous elemental mercury (GEM) at a suburban site in eastern China using generalized additive models. Atmos. Environ. 247, 118181 (2021).
- 37. Schlitzer, R. Ocean data view. odv.awi.de (2023).

Acknowledgements

This work was supported by the National Natural Science Foundation of China (grant nos. 42430410 and 42306248). We thank the China Arctic and Antarctic Administration for fieldwork support. We thank the members of the 13th Chinese National Arctic Research Expedition for their assistance during the fieldwork. We thank the XiaoMi Young Scholar Program for funding support. We acknowledge the NOAA-Air Resources Laboratory (ARL) for developing the HYSPLIT transport and dispersion model. We acknowledge Yaqiang Wang (Chinese Academy of Meteorological Sciences) for developing the meteorological visualization software MeteoInfo.

Author contributions

Z.X. and F.Y. conceived the study. F.Y. performed the field investigation. F.Y. led the original paper writing and methodology with input from Z.X., H.A., and H.L. All authors contributed to data interpretation and writing.

Competing interests

The authors declare no competing interests.

Additional information

Supplementary information The online version contains supplementary material available at https://doi.org/10.1038/s41467-025-61000-z.

Correspondence and requests for materials should be addressed to Fange Yue or Zhouqing Xie.

Peer review information *Nature Communications* thanks Jenny Fisher and the other, anonymous, reviewer(s) for their contribution to the peer review of this work. A peer review file is available.

Reprints and permissions information is available at http://www.nature.com/reprints

Publisher's note Springer Nature remains neutral with regard to jurisdictional claims in published maps and institutional affiliations.

Open Access This article is licensed under a Creative Commons Attribution-NonCommercial-NoDerivatives 4.0 International License, which permits any non-commercial use, sharing, distribution and reproduction in any medium or format, as long as you give appropriate credit to the original author(s) and the source, provide a link to the Creative Commons licence, and indicate if you modified the licensed material. You do not have permission under this licence to share adapted material derived from this article or parts of it. The images or other third party material in this article are included in the article's Creative Commons licence, unless indicated otherwise in a credit line to the material. If material is not included in the article's Creative Commons licence and your intended use is not permitted by statutory regulation or exceeds the permitted use, you will need to obtain permission directly from the copyright holder. To view a copy of this licence, visit https://creativecommons.org/licenses/by-nc-nd/4.0/.

© The Author(s) 2025